

Mixing effects in postdischarge modeling of electric discharge oxygen-iodine laser experiments

Andrew D. Palla, David L. Carroll,^{a)} and Joseph T. Verdeyen
CU Aerospace, Urbana, Illinois 61820

Wayne C. Solomon
University of Illinois at Urbana-Champaign, Urbana, Illinois 61820

(Received 21 October 2005; accepted 16 May 2006; published online 26 July 2006)

In an electric discharge oxygen-iodine laser, laser action at 1315 nm on the $I(^2P_{1/2}) \rightarrow I(^2P_{3/2})$ transition of atomic iodine is obtained by a near resonant energy transfer from $O_2(a^1\Delta)$ which is produced using a low-pressure electric discharge. The discharge production of atomic oxygen, ozone, and other excited species adds higher levels of complexity to the postdischarge kinetics which are not encountered in a classic purely chemical $O_2(a^1\Delta)$ generation system. Mixing effects are also present. In this paper we present postdischarge modeling results obtained using a modified version of the BLAZE-II gas laser code. A 28 species, 105 reaction chemical kinetic reaction set for the postdischarge kinetics is presented. Calculations were performed to ascertain the impact of a two stream mixing mechanism on the numerical model and to study gain as a function of reactant mass flow rates. The calculations were compared with experimental data. Agreement with experimental data was improved with the addition of new kinetics and the mixing mechanism. © 2006 American Institute of Physics. [DOI: 10.1063/1.2215355]

I. INTRODUCTION

Oxygen-iodine laser systems¹ operate on the $I(^2P_{1/2}) \rightarrow I(^2P_{3/2})$ (hereafter denoted I^* and I , respectively) electronic transition of the iodine atom at 1315 nm. The population inversion is produced by the near resonant energy transfer between the metastable excited singlet oxygen molecule, $O_2(a^1\Delta)$ [also denoted $O_2(a)$ hereafter], and the atomic iodine ground state. There are many system issues having to do with weight, safety, and the ability to rapidly modulate the production of the $O_2(a)$ which have motivated investigations into methods to produce significant amounts of $O_2(a)$ using flowing electric discharges. Several investigations have been conducted into the possibility of a continuous flow hybrid electrically powered oxygen-iodine laser with electric discharges to produce the $O_2(a)$.²⁻⁹ These studies have shown that flowing electric discharges through oxygen containing mixtures, typically diluted with a rare gas, can produce useful quantities of $O_2(a)$. Recent studies have demonstrated $O_2(a)$ yields greater than 15% using electric discharges,^{4,5,7-9} gain,¹⁰⁻¹² and cw laser power.^{13,14} Several modeling studies^{2,5,6,15} have also been performed for electric discharge oxygen-iodine laser (ElectricOIL) and similar systems.

Since ElectricOIL development is impacted by an imperfect understanding of postdischarge physics, the BLAZE-II chemical laser model¹⁶ was improved to allow more extensive studies of ElectricOIL postdischarge kinetics and laser performance. In this paper, we present the results of a study with an updated and more comprehensive reaction set than previously utilized.² The impact of a two stream mixing mechanism, defined in terms of diffusion coefficients and a

scheduled mixing approach, is examined. Simulations are compared with experimental data. Also presented is a study of laser gain as a function of reactant mass flow rates.

II. THE BLAZE-II GAS LASER MODEL

The BLAZE-II code¹⁶ was originally written to be as generic a gas laser model as possible. BLAZE-II can treat arbitrary combinations of chemical species characterized by as many as 500 reactions and 40 species. BLAZE-II, which contains one-dimensional fluid dynamic equations whose mixing terms are derived from the two-dimensional (2D) equations that describe the mixing flow field in a gas laser cavity, can be used for axisymmetric and 2D flows. Lasing may occur on a single atomic transition or on as many as ten vibrational bands of a diatomic species. BLAZE-II is capable of performing premixed and mixing calculations. The gain g of an iodine laser is given by¹⁷⁻¹⁹

$$g = \frac{7}{12} \left(\frac{A_{21}\lambda^2}{8\pi} \right) \phi(\nu) \left(N_{I^*} - \frac{1}{2}N_I \right), \quad (1)$$

where $\lambda = 1315$ nm, $A_{21} = 5.0$ s⁻¹, N_{I^*} and N_I are the number densities of excited atomic iodine I^* and ground state atomic iodine I , and the Voigt line shape function $\phi(\nu_0)$ at line center is given by

$$\phi(\nu_0) = \frac{2}{\Delta\nu_D} \left(\frac{\ln 2}{\pi} \right)^{1/2} [1 - \operatorname{erf}(y)] \exp(y^2), \quad (2)$$

where

$$\Delta\nu_D = \frac{2}{\lambda} \sqrt{\frac{2RT \ln 2}{W}} = 1.4492 \times 10^7 \sqrt{T}, \quad (3)$$

^{a)}Author to whom correspondence should be addressed; electronic mail: carroll@cuaerospace.com

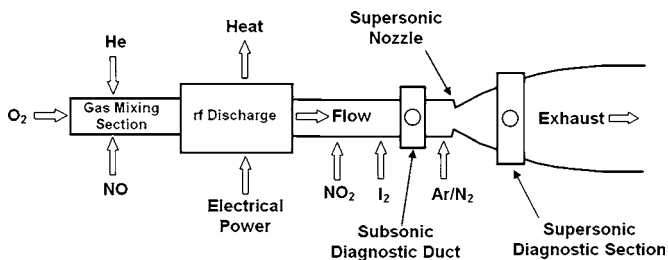


FIG. 1. Schematic of ElectricOIL apparatus that was modeled.

$$y = \frac{\Delta\nu_L}{\Delta\nu_D} \sqrt{\ln 2}, \quad (4)$$

$$\Delta\nu_L = P \sqrt{\frac{T_{\text{ref}}}{T}} \sum_i \alpha_i x_i, \quad (5)$$

where R is the universal gas constant (8.314 J/mol K), W is the molecular weight of iodine (126.9 gm/mol), T is the temperature in Kelvin, T_{ref} is a reference temperature taken to be 295 K, P is the pressure in Torr, x_i is the mole fraction of species i , and the pressure broadening coefficients α_i in MHz/Torr (referenced to 295 K) are 16.2, 7.5, 3.6, 6.2, 10.0, 20.6, and 4.7 for I, O₂, He, N₂, Cl₂, H₂O, and, Ar respectively.^{18,36}

The BLAZE-II code was originally written to model a gas laser in which reactants are injected at a single point. The BLAZE-II code was modified to permit the injection of reactants at an arbitrary number of points at arbitrary locations. This modification allows the code to better model the current ElectricOIL system in which reactants are injected at as many as four positions. Automation was added to the code that allows large parametric studies to be inputted, completed, and reduced quickly. The optimization of the code was substantially improved in order to further reduce run times. BLAZE-II chemical oxygen-iodine laser (COIL) runs using a 33 reaction, 12 species set had previously required ~30 CPU seconds on an IBM RS/6000 machine,²⁰ whereas current BLAZE-II ElectricOIL runs using a 105 reaction, 28 species set now requires ~2 CPU seconds on an Intel Pentium 4 machine and only ~1 CPU second on a Macintosh G5. Code was added to automatically reduce calculation results from multiple cases in large studies. The improvements in optimization and automation have made it possible to complete and quickly analyze large parametric studies on the order of tens of thousands of cases.

The BLAZE-II calculations presented in this paper are based on a four section/injection-point ElectricOIL format,¹¹ with the following sections: (i) discharge output flow, (ii) NO₂ injection, (iii) I₂ injection, and (iv) tertiary diluent (Ar/N₂) injection, as shown in Fig. 1. The flow tube is approximately 4.9 cm in diameter and exhausts through a Mach 2 nozzle. Simulations begin at the exit of the discharge (which is treated as the first reactant section, $X=0$ cm), NO₂ is injected at $X=53$ cm, an I₂/He mixture is injected at $X=81.9$ cm, Ar or N₂ is injected at $X=117.5$ cm, and the nozzle throat is at $X=141.63$ cm. The subsonic diagnostic port, hereafter referred to as the diagnostic port, is at $X=101.9$ cm.

III. BLAZE-II KINETICS SIMULATIONS

The accuracy of BLAZE-II calculations is critically dependent on the accuracy of the input chemical kinetic reaction set. Several I*, O₂($a^1\Delta$), O₂($b^1\Sigma$) [also denoted O₂(b) hereafter], NO, and NO₂ dependent reactions that were not included in previous BLAZE-II ElectricOIL modeling² may affect the accuracy of the model. As such, the chemical kinetic reaction set was expanded to include 28 species and 105 reactions, Table I. Note that a number of temperature dependent reactions have been included because the temperature range in the postdischarge laser system can be as large as 600 K at the exit of the discharge to near 100 K in the supersonic laser cavity. Further, while certain reactions included in the 105 reaction set have rate coefficients that have not yet been measured to a high degree of accuracy, their inclusion in the kinetic package with best available rates increased the agreement of the model with data.

Experiments¹¹ demonstrated the importance of controlling atomic oxygen by titrating with NO₂. Further, the O + NO₂, reaction 84, is highly exothermic²⁵ (1.995 eV) and therefore it is possible that significant fractions of O₂(a) and/or O₂(b) could be produced. As such, reactions 84–86 that include possible branching to O₂(a) and O₂(b) were included in the model. However, premixed predictions of species concentrations and gain as a function of rf power were in the best agreement with data when using a reaction set without branching of reaction 84 to the O₂(a) or O₂(b) states and therefore reactions 85 and 86 were assumed to not occur for the purposes of this study. Further study of reactions 84–86 using the mixing model is planned.

A kinetic study base line case used reactant molar flow rates of O₂:He:NO₂:I₂=4:16:0.2:0.008 mmol/s and assumed a 400 W rf discharge producing O₂(a):O₂(b):O flow rates of 0.48:0.0086:0.32 mmol/s at $X=0$ cm and a total pressure of 12.6 Torr. The O₂(a), O₂(b), and atomic oxygen flow rates are based on experimental data.¹¹ The three-body quenching of O₂(a) by O₂(X)+O, reaction 98, was added to the model and compared to a base line case without reaction 98; a plot of the concentration of O₂(a) as a function of axial position was found to decrease by approximately 5% after 50 cm. The effect of reaction 98 was found to be much more significant in Refs. 7 and 23; we believe this is a consequence of their flow conditions being much slower than ours, 630 cm/s versus 2762 cm/s. The importance of the internal production of NO₂ by the three-body recombination reactions, O+NO+M→NO₂+M, followed by the fast reaction of NO₂ with O is shown in Fig. 2, where the BLAZE-II base line case with reactions 84–86 and 95–98 included was compared with a case that also included the three-body recombination, reaction 100, where M is He. As shown there, the presence of this reaction makes a dramatic difference in the predicted atomic oxygen concentration downstream of the discharge. The majority of the decrease in atomic oxygen in the absence of reaction 100, Fig. 2, is due to the three-body reaction where M is O₂(X), reaction 99. The deactivation reactions 95–97 were included in separate calculations of I*, I*, and O₂(b) concentrations, respectively, and plots of these species concentrations were found to change less than 1%

TABLE I. BLAZE-II ElectricOIL 105 reactions, 28 species set, and reaction rates. Reaction rates for three-body reactions have units of $\text{cm}^6/\text{molecule}^2 \text{ s}$. Certain specified quenching reactions have been assumed from other known reactions.

k	Reaction						Rate ($\text{cm}^3/\text{molecules s}$)	Ref.	
1	$\text{O}_2(^1\Delta)$	+	$\text{O}_2(^1\Delta)$	\rightarrow	$\text{O}_2(^1\Sigma)$	+	O_2	$9.8 \times 10^{-28} T^{3.8} \exp(700/T)$	26
2	$\text{O}_2(^1\Delta)$	+	$\text{O}_2(^1\Delta)$	\rightarrow	O_2	+	O_2	1.7×10^{-17}	26
3	O_2	+	$\text{O}_2(^1\Sigma)$	\rightarrow	$\text{O}_2(^1\Delta)$	+	O_2	3.7×10^{-17}	27
4	$\text{O}_2(^1\Sigma)$	+	H_2O	\rightarrow	$\text{O}_2(^1\Delta)$	+	H_2O	6.7×10^{-12}	26
5	$\text{O}_2(^1\Sigma)$	+	Cl_2	\rightarrow	$\text{O}_2(^1\Delta)$	+	Cl_2	2.0×10^{-15}	26
6	$\text{O}_2(^1\Sigma)$	+	He	\rightarrow	$\text{O}_2(^1\Delta)$	+	He	1.0×10^{-17}	26
7	$\text{O}_2(^1\Sigma)$	+	Ar	\rightarrow	$\text{O}_2(^1\Delta)$	+	Ar	1.0×10^{-17}	From 6
8	$\text{O}_2(^1\Sigma)$	+	Xe	\rightarrow	$\text{O}_2(^1\Delta)$	+	Xe	1.0×10^{-17}	From 6
9	O_2	+	$\text{O}_2(^1\Delta)$	\rightarrow	O_2	+	O_2	8.2×10^{-19}	27
10	$\text{O}_2(^1\Delta)$	+	H_2O	\rightarrow	O_2	+	H_2O	4.0×10^{-18}	26
11	$\text{O}_2(^1\Delta)$	+	Cl_2	\rightarrow	O_2	+	Cl_2	6.0×10^{-18}	26
12	$\text{O}_2(^1\Delta)$	+	He	\rightarrow	O_2	+	He	8.0×10^{-21}	26
13	$\text{O}_2(^1\Delta)$	+	Ar	\rightarrow	O_2	+	Ar	8.0×10^{-21}	From 12
14	$\text{O}_2(^1\Delta)$	+	Xe	\rightarrow	O_2	+	Xe	8.0×10^{-21}	From 12
15	$\text{O}_2(^1\Delta)$	+	N_2	\rightarrow	O_2	+	N_2	1.4×10^{-19}	24
16	$\text{O}_2(^1\Sigma)$	+	N_2	\rightarrow	O_2	+	N_2	2.0×10^{-16}	24
17	$\text{O}_2(^1\Sigma)$	+	N_2	\rightarrow	$\text{O}_2(^1\Delta)$	+	N_2	1.8×10^{-15}	24
18	$\text{O}_2(^1\Sigma)$	+	I_2	\rightarrow	O_2	+	2I	2.8×10^{-11}	35
19	$\text{O}_2(^1\Sigma)$	+	I_2	\rightarrow	$\text{O}_2(^1\Delta)$	+	I_2	2.3×10^{-11}	27
20	$\text{O}_2(^1\Sigma)$	+	I_2	\rightarrow	O_2	+	I_2	6.0×10^{-12}	35
21	$\text{O}_2(^1\Delta)$	+	I_2	\rightarrow	O_2	+	I_2^*	7.0×10^{-15}	26
22	$\text{O}_2(^1\Delta)$	+	I_2	\rightarrow	O_2	+	I_2	5.0×10^{-16}	27
23	I^*	+	I_2	\rightarrow	I	+	I_2^*	$1.4 \times 10^{-13} \exp(1600/T)$	26
24	$\text{O}_2(^1\Delta)$	+	I_2^*	\rightarrow	O_2	+	2I	3.0×10^{-10}	26
25	I_2^*	+	O_2	\rightarrow	I_2	+	O_2	4.9×10^{-12}	28
26	I_2^*	+	H_2O	\rightarrow	I_2	+	H_2O	1.7×10^{-11}	28
27	I_2^*	+	He	\rightarrow	I_2	+	He	9.8×10^{-12}	28
28	I_2^*	+	Ar	\rightarrow	I_2	+	Ar	4.0×10^{-12}	26
29	I_2^*	+	Xe	\rightarrow	I_2	+	Xe	4.0×10^{-12}	From 28
30	I_2^*	+	Cl_2	\rightarrow	I_2	+	Cl_2	6.3×10^{-12}	28
31	I_2^*	+	N_2	\rightarrow	I_2	+	N_2	8.2×10^{-12}	29
32	I	+	$\text{O}_2(^1\Delta)$	\rightarrow	I^*	+	O_2	$2.3 \times 10^{-8} T^{-1}$	26
33	I^*	+	O_2	\rightarrow	I	+	$\text{O}_2(^1\Delta)$	$3.1 \times 10^{-8} T^{-1} \exp(-403/T)$	26
34	I	+	$\text{O}_2(^1\Delta)$	\rightarrow	I	+	O_2	1.0×10^{-15}	26
35	I^*	+	O_2	\rightarrow	I	+	O_2	3.5×10^{-16}	26
36	I^*	+	$\text{O}_2(^1\Delta)$	\rightarrow	I	+	$\text{O}_2(^1\Sigma)$	$4.0 \times 10^{-24} T^{3.8} \exp(700/T)$	26
37	I^*	+	$\text{O}_2(^1\Delta)$	\rightarrow	I	+	$\text{O}_2(^1\Delta)$	1.1×10^{-13}	26
38	I^*	+	I	\rightarrow	I	+	I	1.7×10^{-13}	26
39	I^*	+	H_2O	\rightarrow	I	+	H_2O	2.1×10^{-12}	26
40	I^*	+	He	\rightarrow	I	+	He	5.0×10^{-18}	26
41	I^*	+	N_2	\rightarrow	I	+	N_2	6.5×10^{-17}	30
42	I^*	+	Ar	\rightarrow	I	+	Ar	5.0×10^{-18}	From 40
43	I^*	+	Xe	\rightarrow	I	+	Xe	5.0×10^{-18}	From 40
44	I^*	+	Cl_2	\rightarrow	ICl	+	Cl	5.5×10^{-15}	26
45	I^*	+	Cl_2	\rightarrow	I	+	Cl_2	8.0×10^{-15}	26
46	I^*	+	ICl	\rightarrow	I_2	+	Cl	1.5×10^{-11}	26
47	I_2	+	Cl	\rightarrow	I	+	ICl	2.0×10^{-10}	26
48	ICl	+	Cl	\rightarrow	I	+	Cl_2	8.0×10^{-12}	26
49	I_2	+	2I	\rightarrow	I_2	+	I_2	3.6×10^{-30}	26
50	N_2	+	2I	\rightarrow	N_2	+	I_2	4.2×10^{-33}	31
51	O_2	+	2I	\rightarrow	$\text{O}_2(^1\Delta)$	+	I_2	3.7×10^{-33}	27
52	O_2	+	2I	\rightarrow	O_2	+	I_2	3.3×10^{-32}	27
53	He	+	2I	\rightarrow	He	+	I_2	3.8×10^{-33}	31
54	I_2	+	$\text{I}^* + \text{I}$	\rightarrow	$\text{I}_2(\text{B})$	+	I_2	3.6×10^{-30}	26
55			$\text{I}_2(\text{B})$	\rightarrow	I	+	I	1.0×10^6	26
56	2O	+	He	\rightarrow	O_2	+	He	$4.5 \times 10^{-34} \exp(630/T)$	32
57	2O	+	O_2	\rightarrow	O_2	+	O_2	$4.5 \times 10^{-34} \exp(630/T)$	32
58	2O	+	$\text{O}_2(^1\Delta)$	\rightarrow	O_2	+	$\text{O}_2(^1\Delta)$	$4.5 \times 10^{-34} \exp(630/T)$	32
59	2O	+	Ar	\rightarrow	O_2	+	Ar	$4.5 \times 10^{-34} \exp(630/T)$	From 56–58

TABLE I. (Continued.)

k	Reaction			Rate (cm ³ /molecules s)	Ref.		
60	2O	+	Xe	→ O ₂	+ Xe	$4.5 \times 10^{-34} \exp(630/T)$	From 56–58
61	3O			→ O ₂	+ O	$4.5 \times 10^{-34} \exp(630/T)$	32
62	O	+	O ₂ +He	→ O ₃	+ He	$5.1 \times 10^{-27} T^{-2.8}$	24
63	O	+	2O ₂	→ O ₃	+ O ₂	$5.1 \times 10^{-27} T^{-2.8}$	24
64	O	+	O ₂ +O ₂ (¹ Δ)	→ O ₃	+ O ₂ (¹ Δ)	$5.1 \times 10^{-27} T^{-2.8}$	24
65	O	+	O ₂ +Ar	→ O ₃	+ Ar	$5.1 \times 10^{-27} T^{-2.8}$	From 62
66	O	+	O ₂ +Xe	→ O ₃	+ Xe	$5.1 \times 10^{-27} T^{-2.8}$	From 62
67	2O	+	O ₂	→ O ₃	+ O	$5.1 \times 10^{-27} T^{-2.8}$	24
68	O ₂ (¹ Δ)	+	O	→ O ₂	+ O	2.0×10^{-16}	32
69	O ₂ (¹ Σ)	+	O	→ O ₂ (¹ Δ)	+ O	7.2×10^{-14}	24
70	O ₂ (¹ Σ)	+	O	→ O ₂	+ O	8.0×10^{-15}	24
71	O ₂ (¹ Σ)	+	O ₃	→ 2O ₂	+ O	1.5×10^{-11}	24
72	O ₂ (¹ Σ)	+	O ₃	→ O ₂ (¹ Δ)	+ O ₃	3.3×10^{-12}	24
73	O ₂ (¹ Σ)	+	O ₃	→ O ₂	+ O ₃	3.3×10^{-12}	24
74	O ₂ (ν)	+	O ₂	→ O ₂	+ O ₂	4.0×10^{-14}	24
75	O ₂ (ν)	+	He	→ O ₂	+ He	1.3×10^{-13}	24
76	O	+	O ₃	→ O ₂	+ O ₂	$8.0 \times 10^{-12} \exp(-2060/T)$	24
77	O ₂ (¹ Δ)	+	O ₃	→ 2O ₂	+ O	$5.2 \times 10^{-11} \exp(-2840/T)$	24
78	I ₂	+	O	→ IO	+ I	1.4×10^{-10}	24
79	IO	+	O	→ O ₂	+ I	1.4×10^{-10}	27
80	IO	+	O	→ O ₂ (¹ Δ)	+ I	1.5×10^{-11}	27
81	IO	+	IO	→ O ₂	+ 2I	8.2×10^{-11}	27
82	I	+	O ₃	→ IO	+ O ₂	$2.0 \times 10^{-11} \exp(-890/T)$	24
83	I*	+	O	→ I	+ O	8.0×10^{-12}	35
84	NO ₂	+	O	→ O ₂	+ NO	$6.5 \times 10^{-12} \exp(120/T)$	24
85	NO ₂	+	O	→ O ₂ (¹ Δ)	+ NO	0.0	24
86	NO ₂	+	O	→ O ₂ (¹ Σ)	+ NO	0.0	24
87	O	+	NO	→ NO ₂ *		2.5×10^{-17}	33
88	NO ₂ *			→ NO ₂		5.54×10^{-20}	33
89	O(¹ D)	+	O ₂	→ O	+ O ₂ (¹ Σ)	$2.6 \times 10^{-11} \exp(67/T)$	24
90	O(¹ D)	+	O ₂	→ O	+ O ₂ (¹ Δ)	$1.6 \times 10^{-12} \exp(67/T)$	24
91	O(¹ D)	+	O ₂	→ O	+ O ₂	$4.8 \times 10^{-12} \exp(67/T)$	24
92	O(¹ D)	+	O ₃	→ 2O	+ O ₂	1.2×10^{-10}	24
93	O(¹ D)	+	O ₃	→ O ₂	+ O ₂	1.2×10^{-10}	24
94	O ₂ (¹ Σ)	+	CO ₂	→ O ₂ (¹ Δ)	+ CO ₂	4.1×10^{-13}	24
95	I*	+	NO	→ I	+ NO	1.2×10^{-13}	21
96	I*	+	NO ₂	→ I	+ NO ₂	8.5×10^{-14}	22
97	O ₂ (¹ Σ)	+	NO ₂	→ O ₂ (¹ Δ)	+ NO ₂	4.1×10^{-13}	24
98	O ₂ (¹ Δ)	+	O ₂ +O	→ 2O ₂	+ O	1.0×10^{-32}	23
99	O	+	NO+O ₂	→ NO ₂	+ O ₂	$4.68 \times 10^{-28} T^{-1.5}$	24
100	O	+	NO+He	→ He	+ NO ₂	$2.08 \times 10^{-28} T^{-1.41}$	24
101	O ₂ (¹ Σ)	+	NO	→ O ₂ (¹ Δ)	+ NO	6.0×10^{-14}	24
102	O ₂	+	2NO	→ 2NO ₂		$3.3 \times 10^{-39} \exp(530/T)$	24
103	NO ₂	+	O ₂	→ NO	+ O ₃	$1.8 \times 10^{-12} \exp(1370/T)$	24
104	O ₂ (¹ Δ)	+	CO ₂	→ O ₂	+ CO ₂	2.0×10^{-20}	24
105	O ₂ (¹ Δ)	+	NO ₂	→ O ₂	+ NO ₂	2.0×10^{-20}	From 104

when compared to calculations without these reactions. While the effects of all other new reactions combined resulted in less than a 1% change when compared to calculations without these reactions, these reactions have been included for completeness.

Data showed that although atomic oxygen produced by the rf discharge plays a positive role in the chemistry of the laser by dissociating I₂, it also plays a negative role by quenching I*.¹¹ In order to eliminate the negative effects of atomic oxygen, NO₂ was used to scavenge some of the O atoms upstream of the I₂ injection point, as shown in Fig. 1.¹¹ As such, a numerical study was performed to determine

if we could model the experimental O₂(*a*), I*, and O₂(*b*) concentrations, and gain data as a function of rf discharge power and NO₂ flow rate with the reaction set given in Table I. The calculations used molar flow rates of O₂:He:I₂ = 4:16:0.008 mmol/s and were performed for rf discharge powers from 4 to 800 W (in 4 W increments), for each NO₂ flow rate of 0.0, 0.1, 0.2, 0.5, and 1.0 mmol/s and the case where NO₂ and I₂ flow rates are 0.0 mmol/s, and are presented in Figs. 3–6. These calculations were premixed. The initial O₂(*a*) yield at the exit of the discharge was determined from ElectricOIL O₂(*a*) data¹¹ as a function of rf discharge

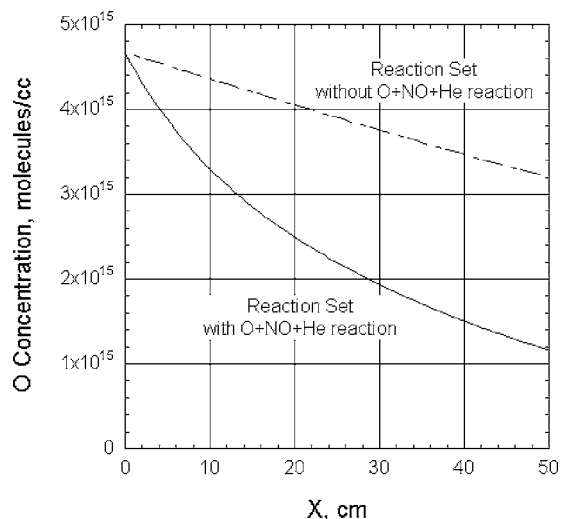


FIG. 2. Base line ElectricOIL mixing predictions of O concentration as a function of axial location with and without the O+NO+He reaction 100, Table I.

power; this data had a peak $O_2(a)$ yield of 12% at 500 W of rf power and flow rates of $O_2:He=4:16$ mmol/s at the diagnostic port position. As discussed above, the $O_2(b)$ flow rate was approximately 1.8% of the $O_2(a)$ flow rate.³⁴ The data from Ref. 11 showed that the production of atomic oxygen in the discharge varied linearly with discharge power such that the atomic oxygen flow rate is approximately 7.5×10^{-4} mmol/s W of discharge power for these flow conditions. The total number of BLAZE-II simulations performed for this set of simulations was 4800, including the modeling of the individual sections for each run.

The NO_2 flow rates used in ElectricOIL and BLAZE-II ElectricOIL calculations are on the order of the O atom flow rate from the discharge. As a result, as discharge power and O atom production are varied as a function of discharge power for a given NO_2 flow rate in the calculations, the equivalence point between the discharge production of atomic oxygen and titration by NO_2 may be crossed. For the purposes of this study, the O/ NO_2 equivalence point is de-

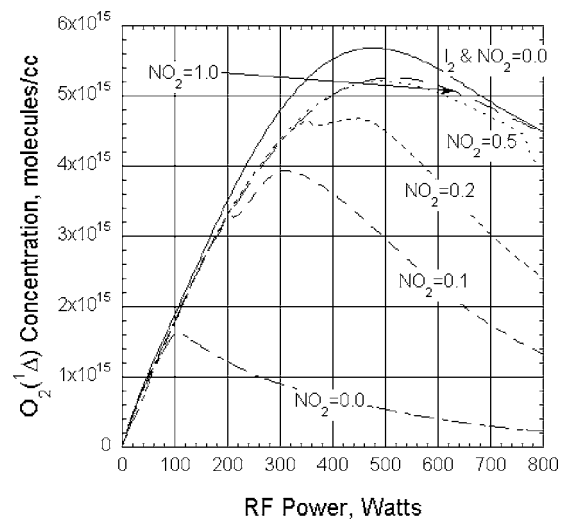


FIG. 3. Premixed predictions of $O_2(^1\Delta)$ concentration at the diagnostic port vs discharge power vs NO_2 flow rate.

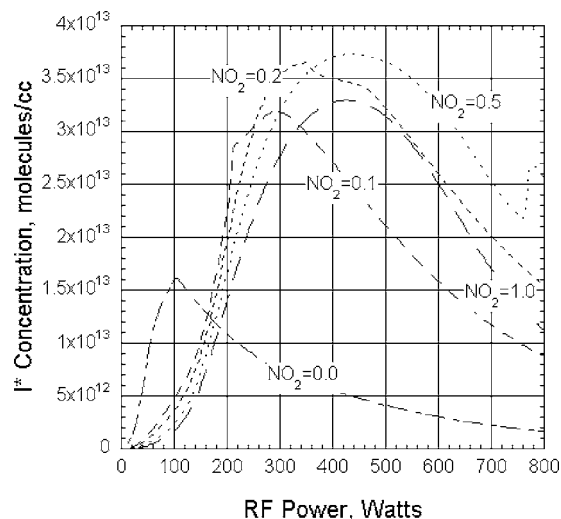


FIG. 4. Premixed predictions of I^* concentration at the diagnostic port vs discharge power vs NO_2 flow rate.

finned for a given NO_2 flow rate as the rf power at which atomic oxygen is produced in the discharge at a rate sufficient to appreciably impact downstream kinetics, despite the removal of atomic oxygen by NO_2 titration and other kinetic processes. In the modeled flow configuration, a quantity of atomic oxygen typically must remain in the flow downstream of the I_2 injection point such that the fast dissociation mechanism of I_2 by atomic oxygen, reactions 78–81, appreciably impacts the downstream kinetics. For example, reactions that are critically dependent upon the presence of atomic oxygen are the fast quenching of I^* by O, reaction 83, and consequently the $I^*+O_2(a) \rightarrow I+O_2(b)$ pooling reaction 36.

As discharge power is varied, dramatic shifts in the behavior of the model are encountered as these equivalence points are crossed. For the cases plotted in Figs. 3–6 with NO_2 flow rates less than or equal to 0.2 mmol/s, the discharge produced flow of O atoms is generally greater than

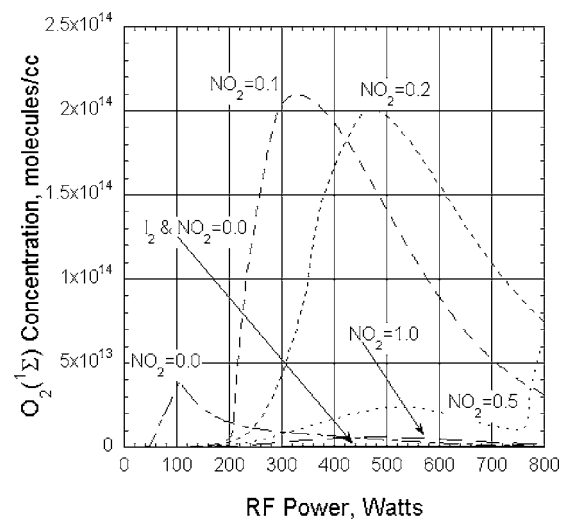


FIG. 5. Premixed predictions of $O_2(^1\Sigma)$ concentration at the diagnostic port vs discharge power vs NO_2 flow rate.

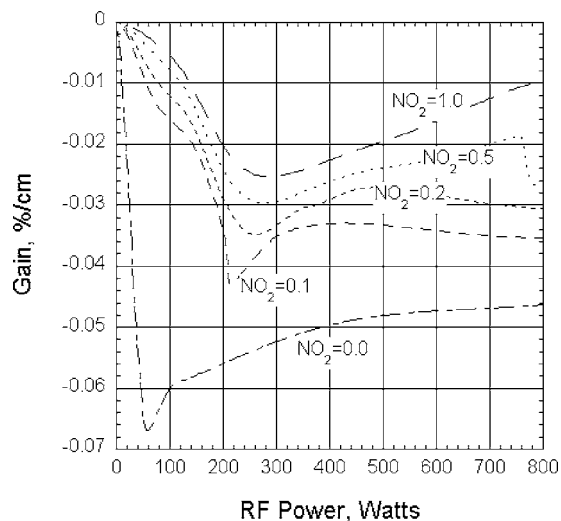


FIG. 6. Premixed predictions of gain at diagnostic port vs discharge power vs NO_2 flow rate.

the NO_2 flow rate for most simulated discharge powers. It should be noted, however, that a NO_2 flow rate less than the discharge produced atomic oxygen flow rate may still act to completely remove the discharge produced atomic oxygen from the flow by “recycling” of the NO_2 via reactions 84–86 and the subsequent three-body NO recombination reactions 99 and 100. This recycling process is slower than the atomic oxygen removal by full or overtitration with NO_2 . In cases with a NO_2 flow rate of 0.5 mmol/s, the discharge production of O atoms is less than the NO_2 flow rate for discharge powers less than approximately 630 W. For cases with a NO_2 flow rate of 1.0 mmol/s, the discharge produced flow of O atoms is less than the NO_2 flow rate for all studied discharge powers. In the premixed calculations, the equivalence points for NO_2 flow rates of 0.1, 0.2, and 0.5 mmol/s occur at rf powers of approximately 300, 450, and 750 W of rf power. These points are characterized by a sharp divergence of behavior between concentration and gain curves for the given NO_2 flow rate and the curves for the next largest NO_2 flow rate, Figs. 3–6, particularly as seen in $\text{O}_2(a)$ concentration curves, Fig. 3.

For comparative purposes, the corresponding experimental data from Ref. 11 are illustrated here in Figs. 7–10. If we compare Figs. 3–6 directly with Figs. 7–10, respectively, it becomes clear that there are both many similarities as well as some significant differences.

- (1) There are strong qualitative similarities in the character of the $\text{O}_2(a)$ curves (Figs. 3 and 7) and I^* curves (Figs. 4 and 8) for NO_2 flow rates of 0.0, 0.1, and 0.2 mmol/s. However, for NO_2 flow rates of 0.5 and 1.0 mmol/s there are dramatic differences which are likely due to mixing these larger quantities of NO_2 into the flow instantly, thereby increasing their impact on the downstream kinetics.
- (2) There are qualitative similarities between the $\text{O}_2(b)$ (Figs. 5 and 9) and gain curves (Figs. 6 and 10) for NO_2 flow rates of 0.0, 0.1, and 0.2 mmol/s, but again there are dramatic differences for NO_2 flow rates of 0.5 and

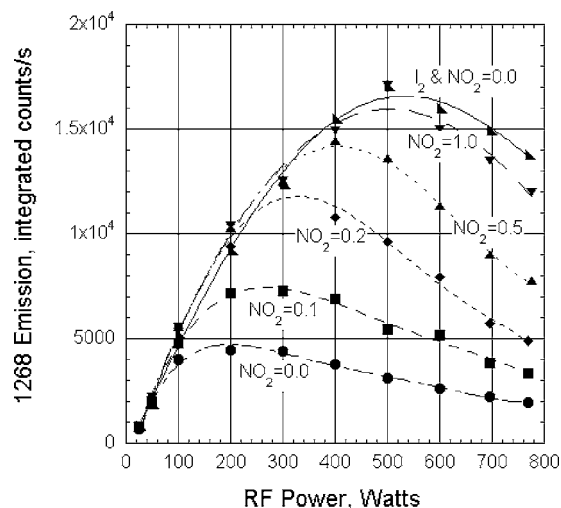


FIG. 7. Experimental $\text{O}_2(^1\Delta)$ emission data from ElectricOIL at the subsonic diagnostic port vs discharge power as a function of NO_2 flow rate, see Ref. 11.

1.0 mmol/s which are also likely due to the premixed nature of the calculations.

- (3) Comparing the $\text{O}_2(b)$ curves (Figs. 5 and 9) shows a significant difference for the $\text{I}_2=0.0$ mmol/s and $\text{NO}_2=0.0$ mmol/s case. In particular, the predicted curve is very weak relative to the predictions for the cases with I_2 and with NO_2 or 0.0, 0.1, and 0.2 mmol/s. This suggests that there may be too much $\text{O}_2(b)$ production via I^* and $\text{O}_2(a)$ pooling, reaction 36, predicted by the model in the presence of iodine.

The most dramatic difference between the calculations and the data is the fact that the model does not predict the correct qualitative behavior for the high NO_2 flow rates of 0.5 and 1.0 mmol/s. Specifically, the $\text{NO}_2=0.5$ and 1.0 mmol/s equivalence points are not crossed as they are in the data. The data shown in Figs. 7–10 suggest that a significant fraction of the I_2 is being dissociated for the $\text{NO}_2=0.5$ mmol/s,

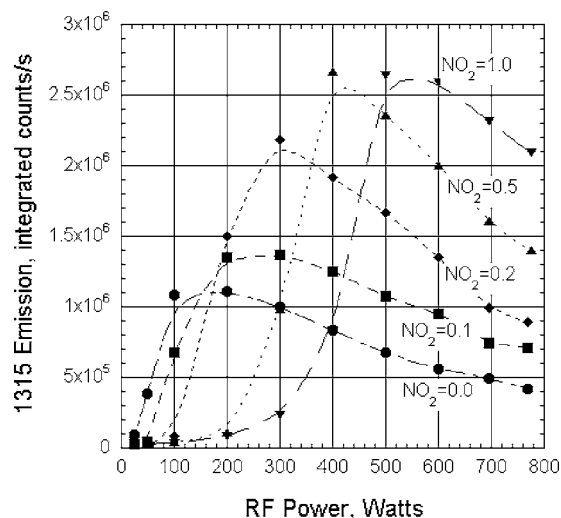


FIG. 8. Experimental I^* emission data from ElectricOIL at the subsonic diagnostic port vs discharge power as a function of NO_2 flow rate, see Ref. 11.

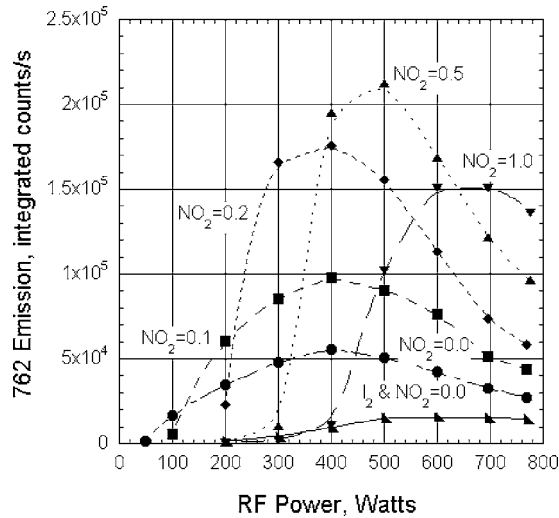


FIG. 9. Experimental $O_2(^1\Sigma)$ emission data from ElectricOIL at the subsonic diagnostic port vs discharge power as a function of NO_2 flow rate, see Ref. 11.

rf power ≥ 300 W cases, and for $NO_2=1.0$ mmol/s, rf power ≥ 400 W cases. Because O atoms are the fastest dissociation mechanism for I_2 , reactions 78–81, and because the character of the 0.5 and 1.0 mmol/s NO_2 calculations do not agree with data, we theorize that the concentration of atomic oxygen is not properly represented in these premixed calculations as a result of some or all of several possible factors.

- (1) All of these simulations were performed as premixed calculations where all injection positions were averaged into the flow discontinuously and the calculation then proceeded downstream as fully mixed. Physically, mixing effects may cause regions of the flow where a larger percentage of atomic oxygen produced in the discharge is allowed to remain unmixed in the downstream flow than in premixed calculations.
- (2) Uncertainties in kinetic rates may affect the downstream concentration of atomic oxygen or other species.
- (3) Experimental diagnostics measuring O atom concentra-

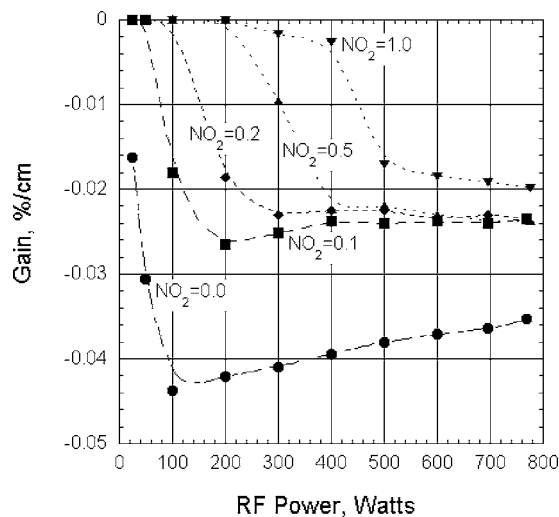


FIG. 10. Experimental gain data from ElectricOIL at the subsonic diagnostic port vs discharge power as a function of NO_2 flow rate, see Ref. 11.

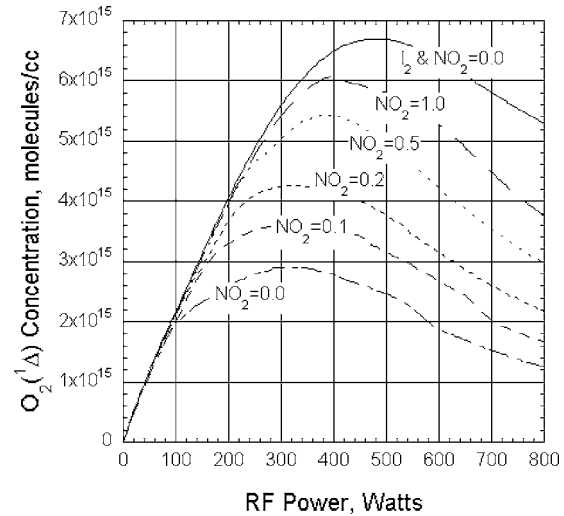


FIG. 11. Mixing predictions of $O_2(^1\Delta)$ concentration at the diagnostic port vs discharge power vs NO_2 flow rate.

tion do not access the entire cross section of the flow, which may not be fully mixed. There is an estimated 15%–20% error associated with the experimental atomic oxygen concentration data, but this error is not sufficient to account for the observed differences at high NO_2 flow rates.

We believe that in a mixing simulation, a more significant quantity of atomic oxygen produced by the discharge may remain in the flow for the requisite distance to interact with the I_2 , thus dissociating the I_2 and influencing other kinetics even when there is a flow of NO_2 higher than the equivalence point. In order to test this theory, the above calculations were repeated with BLAZE configured to use a two-stream mixing model. This mixing model includes diffusion coefficients based on the thermodynamic properties of the reactants and a surface stretching enhancement^{37,38} that uses a simple analytic calculation of the penetration depths of the reactants which are injected transversely to the mean flow. The kinetic theory based laminar diffusion coefficients were scaled by diffusion coefficient multipliers (DCMs) determined via the surface stretching enhancement scheme of Driscoll.^{37,38} The DCMs were based on observed NO_2 and I_2 penetration depth estimates of 0.4 and 1.7 cm, respectively, and were computed to be approximately unity for the NO_2 stream and 2.3 for the I_2 stream. Thus, while the NO_2 mixing was essentially laminar diffusive, the DCM changed the distance required for near complete mixing of the I_2 stream from approximately 40 to approximately 17 cm. Results using the mixing model are presented in Figs. 11–14.

The mixing model predictions for $O_2(a)$, I^* , and $O_2(b)$ concentrations and gain, Figs. 11–14, are in better agreement with data, Figs. 7–10, than premixed model predictions, Figs. 3–6. The equivalence points between NO_2 and atomic oxygen occur at the correct rf power levels in the mixing calculations for each NO_2 flow rate. The rf powers at which the NO_2/O equivalence points occur are tuned by adjusting the NO_2 mixing rate (note that once the mixing rates for NO_2 and I_2 are tuned for a particular set of flow rates, the mixing

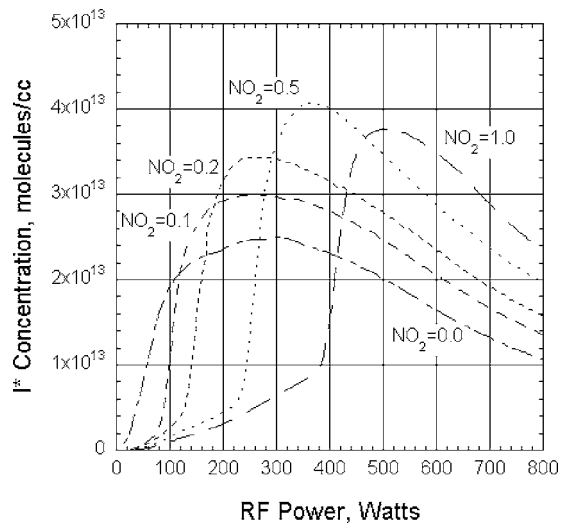


FIG. 12. Mixing predictions of I^* concentration at the diagnostic port vs discharge power vs NO_2 flow rate.

adjustment factor was then held fixed for all other NO_2 flow rates). The mixing model predictions for the relative magnitudes of I^* and $\text{O}_2(b)$ concentrations as a function of NO_2 flow rate, Figs. 12 and 13, are in significantly better agreement with data, Figs. 8 and 9, than are the premixed predictions, Figs. 4 and 5. However, the mixing model still appears to overpredict the concentration of $\text{O}_2(b)$ as a function of NO_2 flow rate and rf power with iodine in the flow with respect to the case without iodine and without NO_2 (I_2 , $\text{NO}_2=0.0$ mmol/s). Since the primary kinetic pathway sustaining $\text{O}_2(b)$ concentration in the flow is $\text{O}_2(a)$ and I^* pooling to $\text{O}_2(b)$, reaction 36, and since the uncertainty in the experimental I_2 flow rate is large, either an error in the input I_2 flow rate or the reaction rate k_{36} (or a combination of both) could explain this error. Although the rate of reaction 36 is well measured, e.g., $k_{36}=(1.3\pm 0.4)\times 10^{-13}$ at $T=353$ K, a simulation of all of the mixing cases studied (in the range of 0–800 W of rf power) using a k_{36} at the lower bound of the rate uncertainty eliminates approximately 1/3 of the previ-

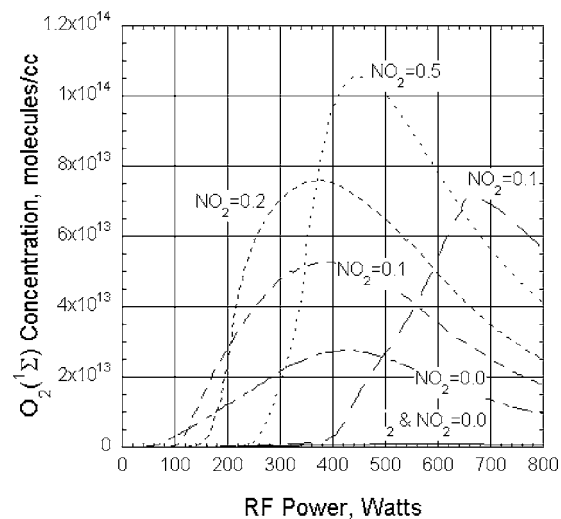


FIG. 13. Mixing predictions $\text{O}_2(^1\Sigma)$ concentration at the diagnostic port vs discharge power vs NO_2 flow rate.

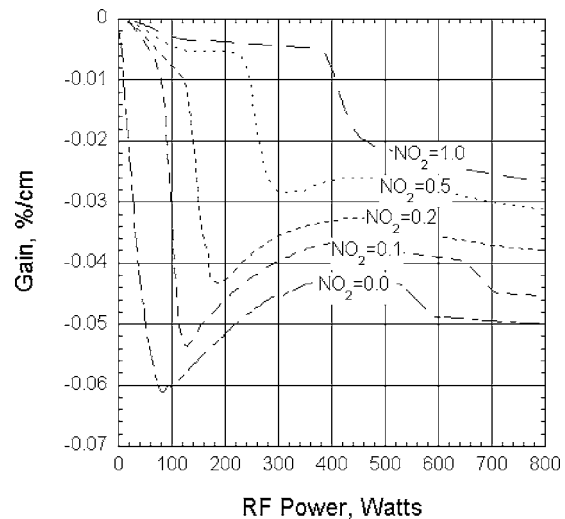


FIG. 14. Mixing predictions of gain at the diagnostic port vs discharge power vs NO_2 flow rate.

ously mentioned $\text{O}_2(^1\Sigma)$ discrepancy between the cases with I_2 and the case without I_2 (not shown for brevity). However, the uncertainty in reaction 36 alone could not explain the observed discrepancy and the more likely source of error is the uncertainty in the I_2 flow rate. To avoid performing a curve fitting exercise in this work, the rate provided in the literature and the measured I_2 flow rate are used throughout the paper. The mixing model predictions for the absolute magnitudes of gain as a function of NO_2 flow rate and rf power, Fig. 14, are also in better agreement with data, Fig. 10, than are the premixed model predictions, Fig. 6. Overall, the mixing model predictions for $\text{O}_2(a)$, I^* , and $\text{O}_2(b)$ concentrations and gain as a function of NO_2 flow rate and rf power are in very good agreement with data indicating that mixing effects are a critical component of ElectricOIL simulations. Agreement between the BLAZE-II model and data may be further improved by continued study of critical kinetics and more accurate determination of input conditions, discharge atomic oxygen yield, and I_2 flow rate, in particular.

IV. BLAZE-II GAIN AND POWER PREDICTIONS

BLAZE-II mixing calculations were performed with the 28 species, 105 reaction set to model current ElectricOIL gain data as a function of I_2 flow rate. Cases modeled used reactant flow rates of $\text{O}_2:\text{He}:\text{NO}$ of 3:16:0.15 mmol/s with I_2 flow rates of 0.008, 0.014, and 0.036 mmol/s at a total pressure of 12.6 Torr. This set of flow conditions was chosen for gain and power modeling because more precise gain data in the supersonic laser cavity were available for these conditions. Simulations assumed 450 W of rf discharge power. The $\text{O}_2(a)$ yield at the exit of the discharge was determined from ElectricOIL data¹⁴ for $\text{O}_2:\text{He}:\text{NO}=3:16:0.15$ mmol/s flow conditions at 450 W of rf discharge power. Atomic oxygen yield was estimated at 450 W of rf power from NO_2 titration experiments³⁴ for the above conditions with NO in the discharge and a numerical study. Estimates³⁴ from titration experiments indicate that the O atom flow rate is ~ 0.13 mmol/s at the NO_2 injectors. Calculations were performed for various discharge atomic oxygen yields and it

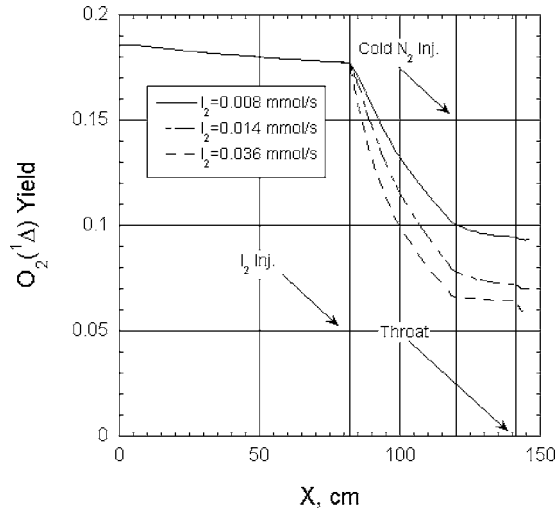


FIG. 15. Mixing predictions of $O_2(^1\Delta)$ yield as a function of axial position vs I_2 flow rate, $O_2:He:NO:N_2=3:16:0.15:55$ mmol/s.

was determined that an O flow rate of 0.25 mmol/s at $X=0$ cm simultaneously provided reasonable agreement with cavity gain data and O atom flow rate estimates at the NO_2 injectors.

All of the simulations discussed in this section used the same mixing parameters determined in Sec. III. For the flow conditions discussed above with a rf power of 450 W, the predicted $O_2(a)$ yield as a function of distance from the discharge exit is shown in Fig. 15 for three different I_2 flow rates. There are four interesting features that are observed in Fig. 15.

- (1) The initial drop in $O_2(a)$ yield occurring until I_2 injection is due to the three-body quenching $O_2(a)+O_2+O \rightarrow O_2+O_2+O$, reaction 98; the pooling reaction $O_2(a)+O_2(a) \rightarrow O_2(b)+O_2$, reaction 1; and quenching by O, O_3 , and $O_2(a)$, reactions 68, 77, and 2, respectively, in order of significance.
- (2) Higher I_2 flow rates result in lower $O_2(a)$ yields downstream in the laser cavity, which is in large part due to the effects of the I^*+O quenching, reaction 83, because the atomic oxygen concentration at the I_2 injection point is still approximately 30% of the discharge exit value.
- (3) The decrease in yield decay after the cold N_2 injection occurs in part from the $O_2(b)+N_2 \rightarrow O_2(a)+N_2$ deactivation channel, reaction 17, where new $O_2(b)$ has been created via $O_2(a)+I^* \rightarrow O_2(b)+I$, reaction 36, after the iodine injection position. There is also an effect from the temperature dependence of reactions 1 and 17.
- (4) The yield after the nozzle throat drops as the equilibrium between the pumping reaction 32 and the reverse pumping reaction 33 shifts further in favor of I^* as the temperature drops in the supersonic expansion, which subsequently increases the rate of energy loss through the I^*+O energy channel.

Figures 16 and 17 illustrate the predicted gain for these three I_2 flow rates. A large drop in gain (increase in absorption) is observed between the I_2 injection location and the N_2 injection location, which is due to the I^*+O quenching

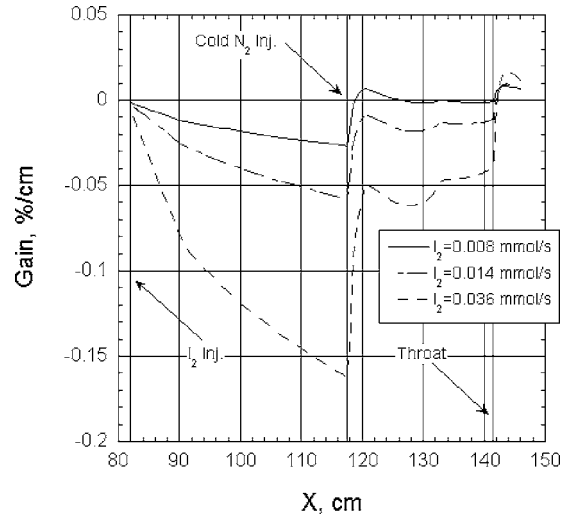


FIG. 16. Mixing predictions of gain as a function of axial position vs I_2 flow rate, $O_2:He:NO:N_2=3:16:0.15:55$ mmol/s.

that ultimately reduces both the I^* and $O_2(a)$ concentrations. There is a sudden rise in gain when the cold N_2 is injected, which is a consequence of the pumping reaction 32 favoring colder temperatures; note that the gain then lowers as heat is transferred from the warmer wall to the cooler flow between N_2 injection position and the nozzle throat (BLAZE-II includes a first order wall heat transfer term). Downstream of the throat the gain increases significantly in the supersonic cavity, Fig. 17. For I_2 flow rates of 0.008, 0.014, and 0.036 mmol/s, the peak gain in the nozzle is predicted to be approximately 0.0085%/cm, 0.0095%/cm, and 0.0168%/cm, respectively. As shown in Fig. 17, the prediction of gain for both the 0.008 mmol/s of I_2 and the 0.036 mmol/s of I_2 cases are in reasonably good agreement with the measured gains¹³ of 0.0067%/cm and 0.0156%/cm, respectively, for these conditions.

Power calculations (not shown for brevity) were run for the above gain cases. The predicted powers were a factor of 2–4 times larger than the measured powers despite the fact

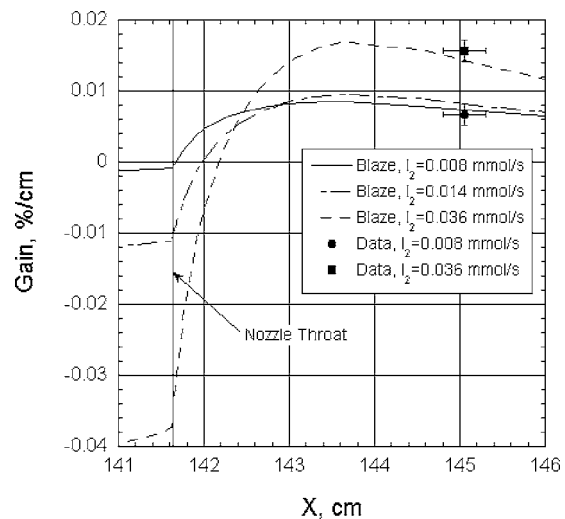


FIG. 17. Mixing predictions of cavity gain as a function of axial position vs I_2 flow rate, $O_2:He:NO:N_2=3:16:0.15:55$ mmol/s.

that the gain was well predicted. We believe that this is likely a problem related to the limited dimensionality of the model. The model assumes flow uniformity across the nozzle and therefore does not account for effects such as a thermal boundary layer that would change the temperature of the nozzle top to bottom. The gain is strongly dependent on temperature; therefore the real device would likely have a gain variation in the vertical direction. The gain data shown in Figs. 16 and 17 were taken along the center of the nozzle flow. If the gain data shown are the peaks of the vertical gain profiles, then the real laser would produce a power output based more on a lower average gain through the laser mode volume. Hence while BLAZE-II is predicting the centerline gain values very well, it is not accounting for higher dimensional effects in the real laser system. Therefore if BLAZE-II gain data were compared to data for average gain across the height of the cavity, a discrepancy comparable to the one in calculated powers would likely be seen. While off-centerline supersonic gain data are not available for the exact flow conditions modeled, gain data taken for similar flow conditions using a 14-pass Herriott optical cell configuration (which sampled the flow both vertically and horizontally) were typically 25%–50% of the magnitude of the gain data taken with a four-pass White optical cell (which only sampled the flow centerline horizontally).³⁹ Investigation of this with a higher dimensional model along with taking more experimental gain measurements to establish a vertical gain profile is recommended.

V. CONCLUDING REMARKS

Recent studies with the ElectricOIL system where the $O_2(a^1\Delta)$ was produced in a flowing electric discharge have demonstrated $O_2(a^1\Delta)$ yields greater than 15%, positive gain, and cw laser power. To better understand the postdischarge physics, premixed and mixing calculations were performed using the generic gas laser model BLAZE-II. BLAZE-II was adapted to allow the multiple sections/injection points of reactants used by ElectricOIL and was enhanced to allow large parametric studies. The BLAZE-II kinetics set was significantly updated and now includes 105 reactions and 28 species.

Premixed simulations were run with the updated BLAZE-II model and compared with experimental data; many of the trends in the data were modeled reasonably well, but simulations with high NO_2 flow rates were dramatically different. We believe that these simulations did not properly represent the concentration of atomic oxygen in the flow tube principally as a result of using premixed flow simulation rather than mixing simulations. The use of a two stream mixing model provided results that were in significantly better agreement with experimental data for I^* , $O_2(a^1\Delta)$, and $O_2(b^1\Sigma)$ concentrations, and gain at the diagnostic port as a function of discharge power and NO_2 flow rate. We believe that a more accurate understanding of the discharge production of atomic oxygen, kinetic rates [e.g., the I^*+O quenching reaction and the $NO_2+O \rightarrow O_2(X^3\Sigma, a^1\Delta, b^1\Sigma)+NO$ branching ratio], and experimental I_2 flow rates may further

improve the accuracy of future BLAZE-II calculations in this respect.

BLAZE-II was used with the 105 reaction, 28 species set to model current ElectricOIL gain data as a function of I_2 flow rate. Atomic oxygen yield in the simulated ElectricOIL conditions was estimated to be 0.25 mmol/s at 450 W of rf power by base lining the model to NO_2 titration experiment results and gain data. For the $I_2=0.008$ and 0.036 mmol/s cases, the gain in the supersonic cavity was modeled well by BLAZE-II.

Overall the BLAZE-II model with the inclusion of mixing effects appears to be predicting many of the observed qualitative trends that have been measured, and several quantitative comparisons to data are reasonable. However, we believe that improvements can be made to the modeling, especially with the use of higher dimension mixing models. Improvements in the knowledge of the kinetics will likely also play a crucial role in better modeling of the system.

ACKNOWLEDGMENTS

This work was supported by the Missile Defense Agency (MDA) through the U.S. Army Space and Missile Defense Command (USA/SMDC) and the Air Force Office of Scientific Research (AFOSR). The authors would like to acknowledge the contributions of T. Madden and G. Hager (Air Force Research Laboratory); M. Kushner (Iowa State University); L. Sentman (University of Illinois); T. Rawlins, S. Davis, and W. Kessler (Physical Sciences Inc.); M. Heaven and K. Morokuma (Emory University); G. Perram (Air Force Institute of Technology); M. Berman (AFOSR); J. Mulroy (MDA); B. Otey (USA/SMDC); and T. Rakhimova and Yu. Mankelovich (Lomonosov Moscow State University).

¹W. McDermott, N. Pchelkin, D. Benard, and R. Bousek, *Appl. Phys. Lett.* **32**, 469 (1978).

²D. L. Carroll, J. T. Verdeyen, D. M. King, B. S. Woodard, L. W. Skorski, J. W. Zimmerman, and W. C. Solomon, *IEEE J. Quantum Electron.* **39**, 1150 (2003).

³D. L. Carroll, J. T. Verdeyen, D. M. King, B. S. Woodard, J. W. Zimmerman, L. W. Skorski, and W. C. Solomon, presented at the AIAA 34th Plasmadynamics and Lasers Conference, Orlando, FL, June 2005 (unpublished), Paper No. 2003-4029.

⁴J. Schmiedberger, S. Hirahara, Y. Ichinoche, M. Suzuki, W. Masuda, Y. Kihara, E. Yoshitani, and H. Fujii, *Proc. SPIE* **4184**, 32 (2001).

⁵A. E. Hill, in *Proceedings of the International Conference on Lasers 2000*, edited by V. Corcoran and T. Corcoran, (STS, McLean, VA, 2001), pp. 249–258.

⁶A. A. Ionin, Y. M. Klimachev, A. A. Kotkov, I. V. Kochetov, A. P. Napartovich, L. V. Seleznev, D. V. Sinitsyn, and G. D. Hager, *J. Phys. D* **36**, 982 (2003).

⁷T. V. Rakhimova *et al.*, presented at the AIAA 36th Plasmadynamics and Lasers Conference, Toronto, ON, June 2005 (unpublished), Paper No. 2005-4918.

⁸W. T. Rawlins, S. Lee, W. J. Kessler, L. G. Piper, and S. J. Davis, presented at the AIAA 36th Plasmadynamics and Lasers Conference, Toronto, ON, June 2005 (unpublished), Paper No. 2005-5299.

⁹Yu. V. Kolobyanin *et al.*, presented at the AIAA 36th Plasmadynamics and Lasers Conference, Toronto, ON, June 2005 (unpublished), Paper No. 2005-4920.

¹⁰D. L. Carroll *et al.*, *Appl. Phys. Lett.* **85**, 1320 (2004).

¹¹D. L. Carroll *et al.*, *IEEE J. Quantum Electron.* **41**, 213 (2005).

¹²W. T. Rawlins, S. Lee, W. J. Kessler, and S. J. Davis, *Appl. Phys. Lett.* **86**, 051105 (2005).

¹³D. L. Carroll *et al.*, *Appl. Phys. Lett.* **86**, 111104 (2005).

¹⁴D. L. Carroll *et al.*, *IEEE J. Quantum Electron.* **41**, 1309 (2005).

- ¹⁵D. S. Stafford and M. J. Kushner, *J. Appl. Phys.* **96**, 2451 (2004).
- ¹⁶L. H. Sentman, M. Subbiah, and S. W. Zelazny, "BLAZE II: A chemical laser simulation computer program," Bell Aerospace Textron Technical Report No. H-CR-77-8 1977 (unpublished).
- ¹⁷K. A. Truesdell, S. E. Lamberson, and G. D. Hager, presented at the AIAA 23th Plasmadynamics and Lasers Conference, Nashville, TN, June 1992 (unpublished), Paper No. 992-3003.
- ¹⁸P. G. Crowell and D. N. Plummer, *Proc. SPIE* 1871, **1871**, 148 (1993).
- ¹⁹P. G. Crowell, RDA Report No. 87-A/K-3-02-1079, 1989 (unpublished).
- ²⁰D. L. Carroll, *AIAA J.* **33**, 1454 (1995).
- ²¹M. C. Heaven, 23 April 2004 (private communication).
- ²²J. Han, S. P. Tinney, and M. C. Heaven, *Proc. SPIE* **5448**, 261 (2004).
- ²³T. V. Rakhimova *et al.*, presented at the AIAA 36th Plasmadynamics and Lasers Conference, Toronto, ON, June 2005 (unpublished), Paper No. 2005-4918.
- ²⁴R. Atkinson, D. L. Baulch, R. A. Cox, R. F. Hampson, Jr., J. A. Kerr, M. J. Rossi, and J. Troe, *J. Phys. Chem. Ref. Data* **26**, 550 (1997).
- ²⁵I. M. W. Smith, R. P. Tuckett, and C. J. Whitham, *Chem. Phys. Lett.* **200**, 615 (1992).
- ²⁶G. P. Perram and G. D. Hager, Air Force Weapons Laboratory Report No. AFWL-TR-88-50, 1988.
- ²⁷J. Han, A. V. Komissarov, S. P. Tinney, and M. C. Heaven, *Proc. SPIE* **4971**, 45 (2003).
- ²⁸M. C. Heaven, Air Force Office of Scientific Research Report No. AFOSR-TR-95-0012, 1995.
- ²⁹M. C. Heaven, 1996 (private communication).
- ³⁰J. J. Deakin and D. Husain, *J. Chem. Soc., Faraday Trans. 2* **68**, 1603 (1972).
- ³¹G. E. Busch, *IEEE J. Quantum Electron.* **17**, 1128 (1981).
- ³²J. T. Herron and D. S. Green, *Plasma Chem. Plasma Process.* **21**, 459 (2001).
- ³³F. Kaufman, *Proc. R. Soc. London, Ser. A* **247**, 123 (1958).
- ³⁴J. W. Zimmerman and D. M. King, 2005 (private communication).
- ³⁵V. N. Azyazov, I. O. Antonov, S. Ruffner, and M. C. Heaven, *Proc. SPIE* **6101**, 6101C-53 (2006).
- ³⁶S. J. Davis, W. J. Kessler, and M. Bachmann, *Proc. SPIE* **3612**, 157 (1999).
- ³⁷R. J. Driscoll, *AIAA J.* **24**, 1120 (1986).
- ³⁸R. J. Driscoll, *AIAA J.* **25**, 965 (1987).
- ³⁹D. M. King *et al.*, presented at the AIAA 36th Plasmadynamics and Lasers Conference, San Francisco, CA, June 2006 (unpublished), Paper No. 2006-3756.

Journal of Applied Physics is copyrighted by the American Institute of Physics (AIP). Redistribution of journal material is subject to the AIP online journal license and/or AIP copyright. For more information, see <http://ojps.aip.org/japo/japcr/jsp>